Optimization of the flow distribution in a gyrotron cavity using evolutionary CFD simulations driven by a genetic algorithm

Optimization of the flow distribution in a gyrotron cavity using evolutionary CFD simulations driven by a genetic algorithm

Laura Savoldi[1], Andrea Allio[1], Alberto Leggieri[2]

[1] MAHTEP Group, Dipartimento Energia "Galileo Ferraris", Politecnico di Torino, Corso Duca degli Abruzzi 24, 10129 Torino, Italy
[2] THALES Microwave and Imaging Subsystems, 78140 Velizy-Villacoublay, France.

Keywords: Optimization, Genetic Algorithm, Gyrotron cavity, Flow distribution, CFD

List of acronyms	
AMG	Algebraic multigrid
CFD	Computational Fluid Dynamics
ECRH	Electron Cyclotron Resonance Heating
GA	Genetic Agorithm
O/C	Open / Closed
RANS	Reynolds-averaged Navier-Stokes equations
RF	Radio frequency
UI	Uniformity Index

Abstract

The steadily increasing performance requested to gyrotrons, to comply with their function of heating and current drive in fusion reactors, put a progressively increasing burden on the heat removal from the interaction cavity, where the heat flux can easily reach 20 MW/m^2 on its inner surface. The cavity is actively cooled by subcooled water in forced flow in an annular region, and the water flow typically enters and exits through a single inlet and outlet. The high-speed flow entering from the inlet potentially drives an inhomogeneous flow azimuthally in the cavity region, but helps in locally bursting the heat removal due to the impinging effect of the cold-water flow. Here a new design of the water inlet in the cavity region is performed through a simplified genetic algorithm, in such a way that the flow homogeneity in the gyrotron cavity is maximized, without reducing the beneficial cooling due to the impact of the water jet on the cavity wall. The presence of multiple holes feeding the cavity, with their azimuthal location driven by the genetic algorithm, is analyzed through Computational Fluid Dynamics (CFD) simulations. Once the multi-inlet location is optimized, the dimension of the inlet holes is tuned to burst the heat transfer effect, reaching a high level of temperature and flow homogeneity in the cavity.

1. Introduction

In the field of nuclear fusion, the heating of the Deuterium-Tritium plasma, which should reach a temperature of several hundred millions K to self-sustain the fusion reactions in a magnetic-confinement devices, will be obtained (also) through Electron Cyclotron Resonance Heating (ECRH) [1] using gyrotrons [2], microwave-generating devices. A gyrotron is typically made by several components (see Figure 1), of

which the ones with significant relevance for their thermal aspects are: the injection gun [3], producing an annular electron beam; the interaction region [4], where the electric and magnetic fields interact with the electrons and a large part of the electron orbital kinetic energy is converted into the RF output; the RF window [5], providing a barrier between the vacuum side of the gyrotron and the output transmission line, and finally the collector [6,7], which absorbs the heat of the spent electron beam. The interaction region consists of an open-ended waveguide cavity, usually with a circular transverse cross-section. The interaction between the electron beam and the electromagnetic wave results in a high ohmic heating on the inner surface of the resonant cavity, which in turn drives a modification of the output RF frequency, due to the variation of the working conditions of the cavity [8].

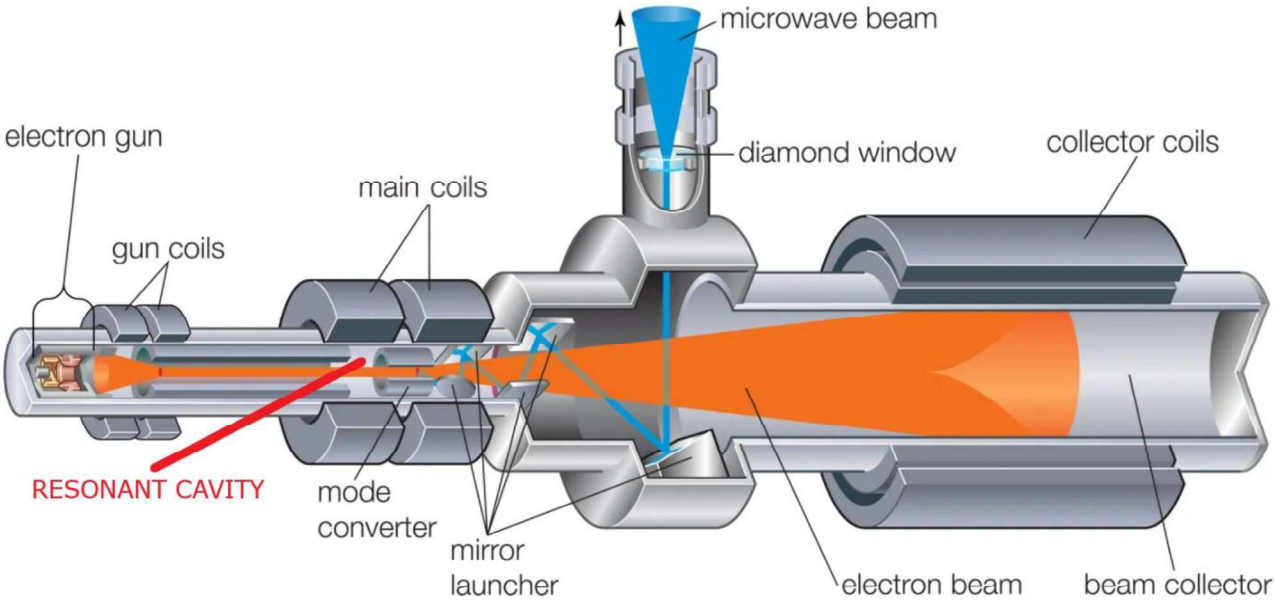

Figure 1 – Schematic view of a gyrotron, with its main components (modified from [9]*)*

The steadily increasing performance requested to gyrotrons, to comply with the their function in fusion reactors [10,11], put a progressively increasing burden on the heat removal from the interaction cavity, which is typically actively cooled by subcooled water in forced flow. In the typical European gyrotron design [12], the water flow enters from a single inlet in a mixing chamber, which can give access through a hole to, or directly acting as, the inlet manifold for the cavity cooling, see Figure 2. To help removing the very high heat load from the cavity wall, which can easily reach values larger than 25 MW/m^2, the annular region around the cavity can be equipped with fins [13,14], mini-channels [15][16] or a sort of porous matrix made by Raschig Rings [17][18,19], mm-size hollow and thin copper cylinders brazed together to provide a highly-conductive porous medium. The coolant flows in the annular region around the resonant cavity, then removes the heat tail from the uptaper and exits from a single outlet pipe as shown in Figure 2. The single inlet (and outlet) of the coolant can potentially drive an azimuthally inhomogeneous flow in the cavity region, which in turn can lead to hot or cold spots around the cavity, jeopardizing the gyrotron performance. From that perspective, a flow distribution as homogenous as possible at the entrance of the cavity region is advisable. Note, however, that, from one other side, the single inlet to the cavity region, forcing all the flow rate to pass through, produces an acceleration of the fluid, with a sort of jet effect of the coolant against the cavity. The water jet obtains larger heat transfer coefficient on the portion of the cavity directly hit by the jet, that helps in keeping locally the cavity temperature much lower than in the rest of the cavity, decreasing the average temperature of the heated surface, notwithstanding the larger temperature non-uniformity resulting for the flow inhomogeneity.

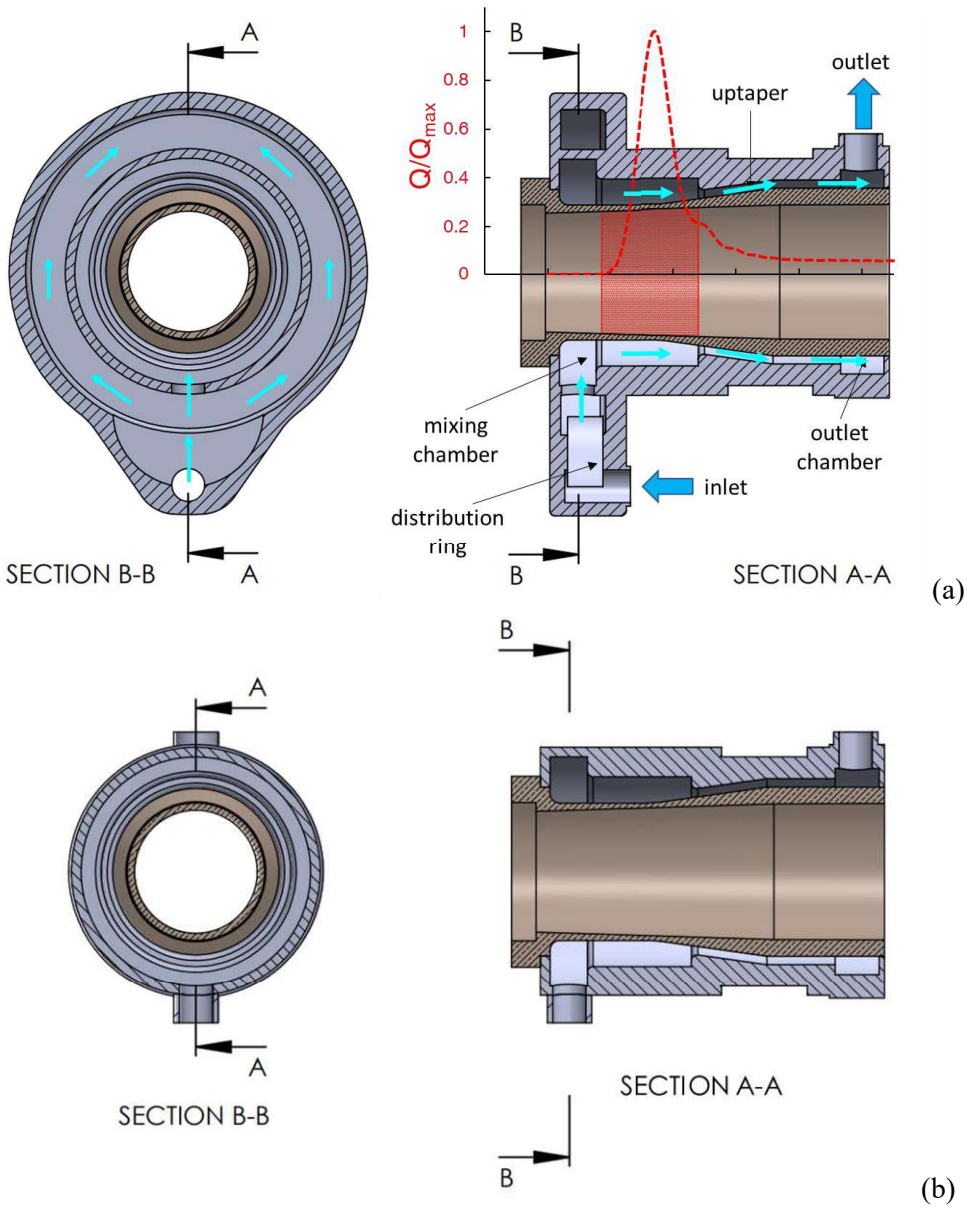

Figure 2 – (a) Frontal section of a gyrotron cavity with distribution ring (at left) and longitudinal section with detail of the heat load deposited on the surface of the cavity (at right). The blue arrows describe the path of the cooling fluid. (b) Section of a gyrotron without distribution ring.

Here we aim at developing a strategy for designing the water inlet in the cavity region, and, at the same time, to develop a novel inlet design to maximize the flow homogeneity in the gyrotron cavity, without reducing the beneficial cooling due to the impact of the water jet on the cavity wall. The proposed design addresses the technical requirements of the Thales TH1507U gyrotron operating at 1.5 MW Continuous Wave [20] that is the direct evolution of the TH1507 140GHz 1 MW gyrotron [21] operating at the Weldenstein W7-X stellerator in Greifswald. The 50 % larger power given by this upgrade reflects in a sensible increase of the ohmic loading in the cavity with the consequent need to improve the heat management by a suitable improvement of the cooling circuit.

The problem is tackled in two steps: first, we address the pure issue of the flow distribution; then we apply the resulting solution, described in [22], by developing a computational model based on a genetic algorithm. This strategy allows to have multiple holes, of different dimensions and at different locations, on the interface wall between the mixing chamber (distribution ring) and the cavity inlet manifold. The interface wall is initially subdivided in several regions, which are progressively automatically opened/closed in evolutionary Computational Fluid Dynamic (CFD) simulations by means of a simplified genetic algorithm (pseudo-genetic GA), targeting the maximum homogenization. Genetic Algorithms are a class of metaheuristic

optimization techniques inspired by the process of natural evolution. In GAs, a population of individual solutions (in the case at hand here, the sequence of open/close holes around the distribution ring) changes during the optimization process. Each individual solution has properties called chromosomes that can be mutated and modified. In each iteration, or generation, the set objective function is evaluated for each individual: the best individuals, more complaint with the target function of the algorithm, are used to produce children for the following generation and the worst individuals are removed. In this way the population evolves towards an optimal solution from generation to generation. The pseudo-genetic GA developed here does not start from a population of totally random individuals, but the initial population is chosen to shorten the generation evolution. The adoption of the pseudo-genetic algorithm allows a significant reduction of the computational effort, driving the choice of the optimal configuration. Once the optimal number and location of inlets is identified, in a second step, the hole dimension is reduced to a value that allows reaching at least the same fluid acceleration in the holes as in the original single-hole configuration, enhancing the cavity cooling by jet effect. The final result, in terms of flow and temperature distribution in the cavity, is compared to the original (single-inlet) one, allowing quantitatively assessing the improvement.

The paper is organized as follows: in section 2, the CFD model used for the analysis of the cavity with multiple coolant inlets is discussed, and in section 3 the methodology for the research of an optimized configuration is presented, together with the selection of the initial population for the GA. The results coming from the evolutionary GA are then reported in Section 4, discussing the optimal configuration that has been found and its implementation in an engineered solution. Section 5 is devoted to the analysis and improvement of the heat transfer enhancement by reducing the size of the inlets, and the conclusion of the whole optimization exercise are drawn in Section 6.

2. CFD model for the gyrotron cavity with multiple fluid inlets

2.1 Computational domain

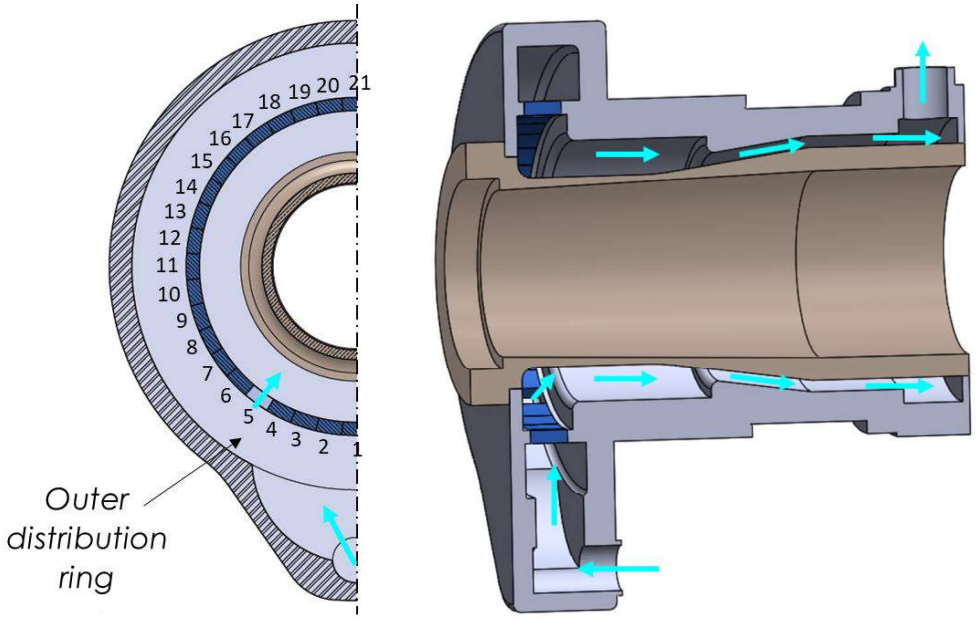

(a) (b)

Figure 3 – 2D (a) and 3D (b) views of the different sectors used in the optimization analysis. In the 2D view, the number of the different sectors is also reported. In both views, sector number 5 is open as an example.

The computational domain adopted here (including only the fluid domain in this first part of the paper) is shown in Figure 4, clearly taking advantage of the symmetry of the cavity. The fluid (subcooled water pressurized at 0.5 MPa) enters the distributor upstream of the cavity form a side feeding pipe. The fluid is then

forced to move azimuthally in the outer distribution ring, and where open sectors are found at the interface to the cavity inlet manifold, the fluid can access the cavity region, as through sector #5 in Figure 4.

The methodology adopted for the design of the shape, dimension and position of the holes in the interface wall between the distribution ring and the inlet mixing chamber is based on the subdivision of the wall in a number N_s of small passages, each corresponding to a given azimuthal extension, see Figure 3. Here we take for the passages the azimuthal extension of 9° (that gives $N_s = 40$) which is a value small enough to check the efficiency of the proposed methodology. The different passages can be considered either "open", i.e. holes available for the fluid flow, or "closed", i.e. walls, according to the local settings of each specific simulation. Each passage, in fact, consists of a volume, separated from the other passages, in which the simulation of the fluid-dynamic problem can be turned on or off. When two neighboring passages are both active, there is a continuity interface between them; when one of the two is deactivated, this interface is replaced by a wall boundary condition.

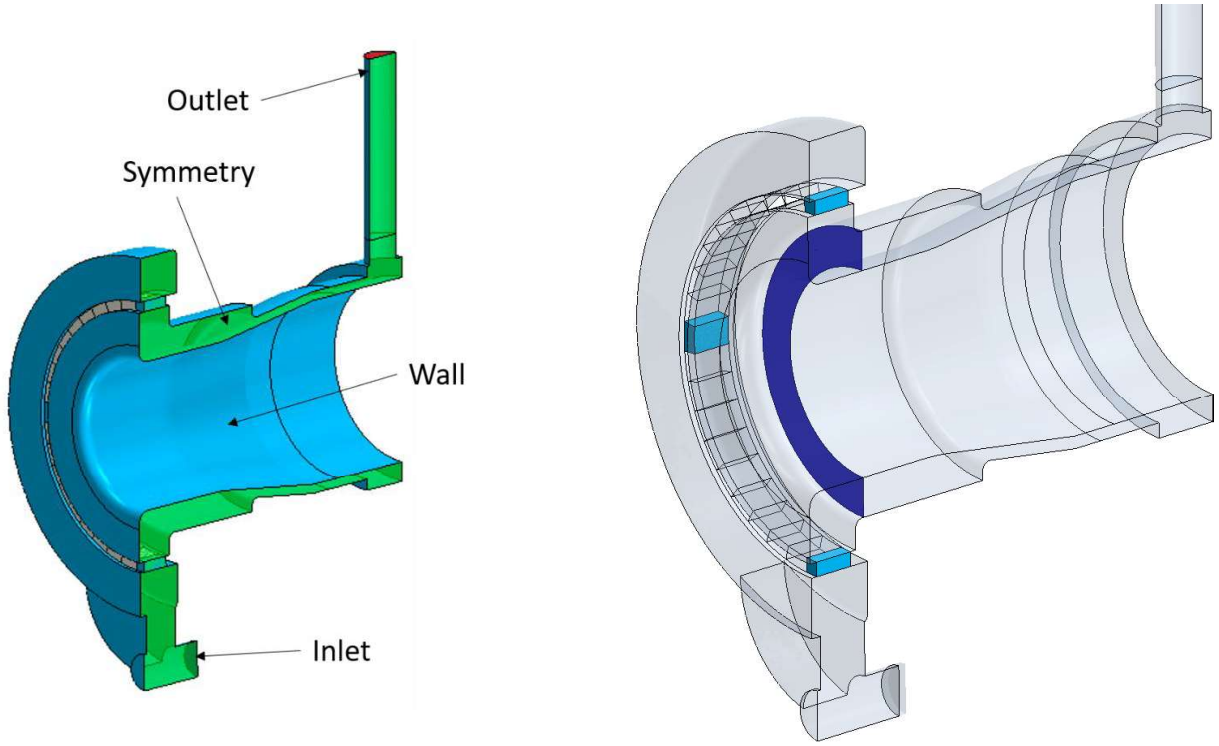

Figure 4 – (a) Computational domain and boundary conditions types adopted for the simulations. (b) In dark blue: detail of the flow section where the Uniformity Index (UI) has been defined, according to Eq. (1); in light blue: detail of the three-dimensional shape of the small sectors.

2.1.1 Fluid model

According to the technical requirements the water flow (50 l/min for the entire cavity, at a pressure set equal to 0.8 MPa at the inlet, and with a reference inlet temperature of 25 °C) is in turbulent conditions not only at the pipe inlet and outlet, where the value of the Reynolds number Re is ~91000, but also all along the cavity. The mass and momentum conservation equations for the fluid flow are solved using a time-averaged approach (Reynolds-averaged Navier-Stokes - RANS - equations) and the turbulent problem is closed using a two-equation SST k-ω model [23]. That closure uses a blending function to combine the benefits of the k-ω model, to better simulate the flow in the viscous sub-layer near the wall, and the k-ε model, to better simulate the bulk flow away from the wall. An all-y+ wall treatment is adopted to allow an automatic switching between low-Re and high-Re approaches.

A second-order scheme with upwind is chosen for the spatial discretization and a segregated flow model, with an Algebraic MultiGrid (AMG) solver, is used to solve the flow equations [24]. The fluid is considered all at the prescribed inlet temperature so that the solution of the energy equation is not required at this stage. The simulations are performed in steady-state, since the time-scales of the propagation of any

pressure disturbance in the domain are much faster than those relevant for the gyrotron operation, targeting an order of magnitude of several hundred seconds in the so called continuous-wave operation.

2.1.2 Mesh

For the hydraulic analysis performed here, a polyhedral mesh has been built with a base size of 0.80 mm everywhere except in the interface wall region and in the annular region between the interface wall and the section highlighted in Figure 4b. In the interface wall region a reduced base size of 0.25 mm has been adopted, driven by the need of having a suitable discretization of the wall region, see Figure 5b. In the above-mentioned annular region, a base size has been 0.5 mm is adopted in order to better describe the change of direction of the fluid flow from radial to axial direction. Out of the interface wall region, prism layers have been inserted to better simulate the velocity gradient at the wall, mainly in the regions where the highest turbulence of the flow regime of the fluid is expected (i.e., regions with reduced flow section).

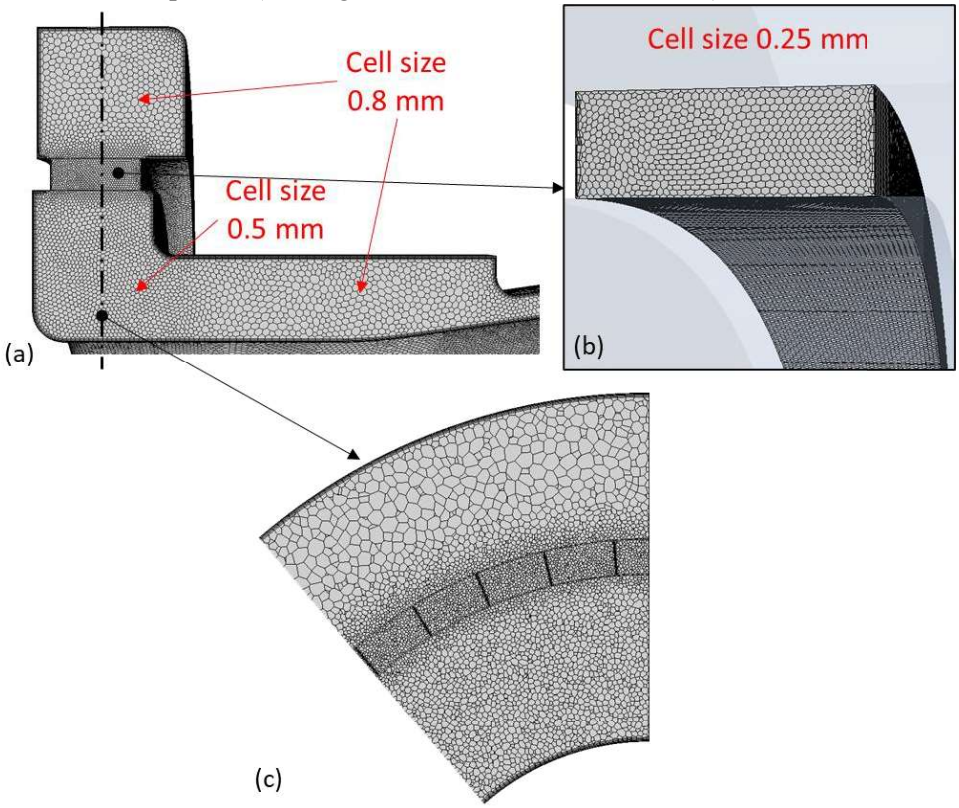

Figure 5 - Detail of the polyhedral mesh for the thermohydraulic simulation of the TH1507U cavity (a), with the details of the passages in the interface wall region (b) and of a cross section (c).

3. Optimization strategy to enhance the flow homogeneity

Evolutionary simulations progressively modify the configuration of the interface wall between the distributing ring and the mixing chamber, by opening and closing each of the passage, to achieve the maximum Uniformity Index (UI) of the axial velocity on the entering section of the high heat load region (see Figure 2) downstream of the interface wall, taken as target functions according to Eq. 1.

$$UI = 1 - \frac{1}{2A_0}\int_{A_0} \frac{|v_z - \overline{v_z}|}{|\overline{v_z}|}\, dA \tag{1}$$

$$\overline{v_z} = \frac{1}{A_0}\int_{A_0} v_z\, dA \tag{2}$$

In Eq. 1, A_0 is the area of the section (see the dark blue surface in Figure 4b), v_z is the axial velocity, $\overline{v_z}$ is the average axial velocity on the section. Just to give a feeling about the value of UI, in case of a single hole for

the inlet it is ~ 0.05, and the axial velocity spans from large positive values (5.5 m/s, hitting the cavity wall) to large negative values (-2.1 m/s) in view of the strong vortex originated by the ingle inlet, see Figure 6.

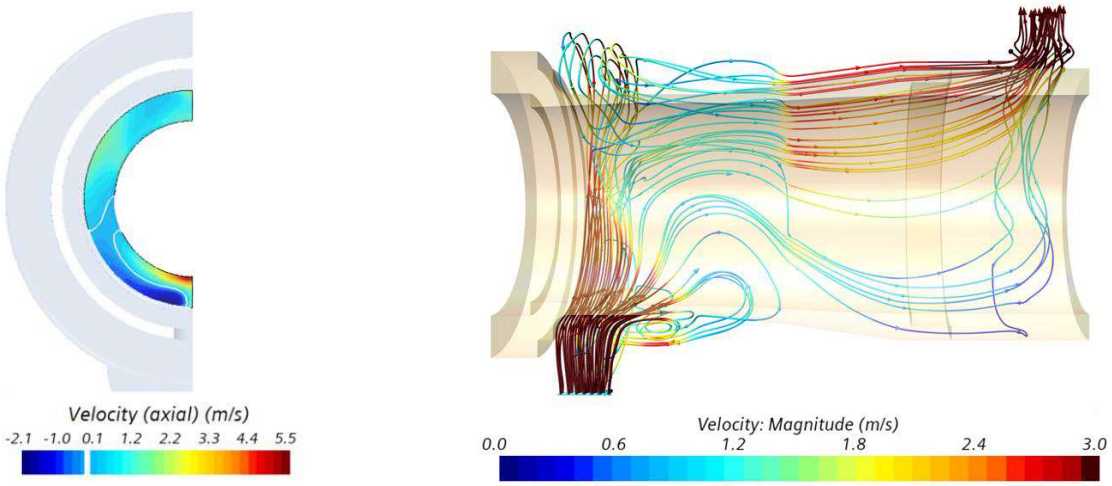

(a) (b)

Figure 6 – (a) Axial velocity distribution computed for the single inlet design on the surface at the inlet of the high heat load region (blue section in Figure 4); the white lines separate the positive and the negative values of the velocity. (b) Streamlines (45 lines uniformly distributed) colored by the value of the fluid velocity for the single inlet model.

The genetic algorithm developed to drive the evolutionary simulations, avoiding the computational burden to perform a full set of 2^{Ns} simulations, starts from the initial population of individuals characterized by the open/closed (O/C) passages for the fluid in the interface wall reported in Table 1, to automatically search the configuration that maximizes the UI. Note that 21 passages are considered on half cavity for symmetry reasons, assuming that the sections 1 and 21 are actually split between the two symmetric halves of the cavity considered here. To enforce the symmetry of the computed flow, the initial population involves possible fluid entrance at an azimuthal position of 0° (passage 1), 90° (passage 11) and 180° (passage 21), including all possible open/closed combinations (except the one with all sections closed, which is trivially not relevant), while all the other passages are kept closed.

Table 1 – Initial population for the optimization analysis through the genetic algorithm, which allows mutations for the flow passages 1, 11 and 21. The blue cells indicate the passages opened for the fluid passage, the white cells those left closed, and the grey cells those closed without any mutation in the first generation.

Flow passage ID →	1	2	3	4	5	6	7	8	9	10	11	12	13	14	15	16	17	18	19	20	21
I1																					
I2																					
I3																					
I4																					
I5																					
I6																					
I7																					
Individual ID ↑																					

The CFD simulations are then performed in sequence for all the cases included in the initial population. The simulation with the highest UI is then automatically selected for the first child generation, freezing the O/C status of the fluid passages 1, 11 and 21. For the first child generation, mutations are allowed only for the fluid passages adjacent to the three used for the definition of the first population, as shown in Table 2 (i.e., passages 2, 10, 12, 20), while all the other passages are kept closed.

Table 2 – First child generation for the optimization analysis through the genetic algorithm, which allows mutations for the flow passages 2, 10, 13 and 20. The pink cell indicate the opening/closure status inherited from the individual of the first generation with the highest UI, the blue cells indicate the passages opened for the fluid passage, the white cells those left closed, and the grey cells those closed without any mutation in the first generation.

Flow passage ID →	1	2	3	4	5	6	7	8	9	10	11	12	13	14	15	16	17	18	19	20	21
I8																					
I9																					
I10																					
I11																					
I12																					
I13																					
I14																					
I15																					
I16																					
I17																					
I18																					
I19																					
I20																					
I21																					
I22																					
I23																					
Individual ID ↑																					

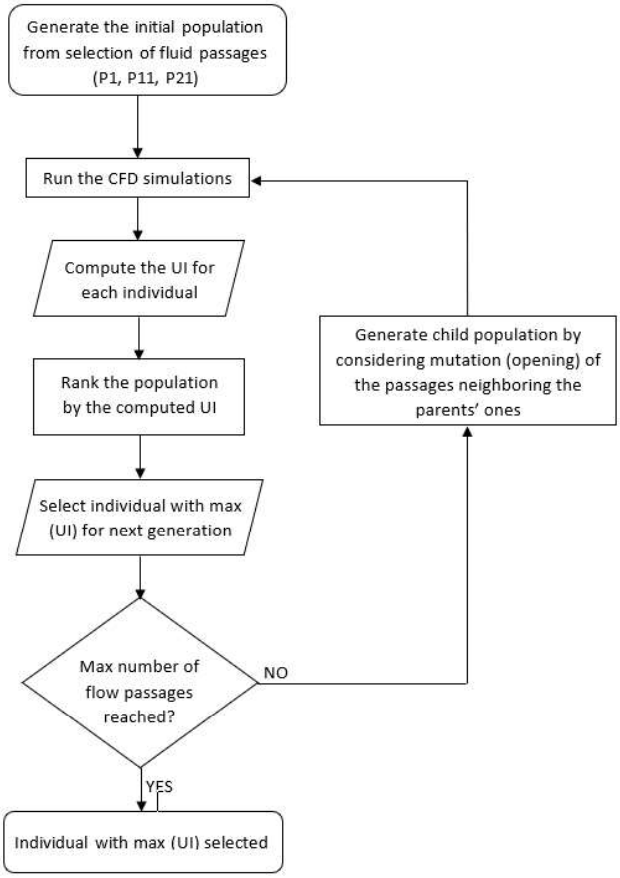

Figure 7 – Optimization approach to get the maximum UI. The evolutionary simulations on all the individuals of the different generations are run automatically.

The algorithm, summarized in Figure 7, goes on automatically defining the following child generations:

- The second child generation plays with the O/C status of the passages 3, 9, 13, 19, starting from the best configuration (maximum UI) found in the first generation,
- The third child generation plays with the O/C status of the passages 4, 8, 14, 18, starting from the best configuration (maximum UI) found in the second generation,
- The fourth child generation plays with the O/C status of the passages 5, 7, 15, 17, starting from the best configuration (maximum UI) found in the third generation,
- The last generation plays only with the O/C status of the passages 6, 16, starting from the best configuration (maximum UI) found in the fourth generation.

Note that here the same configuration is considered more than once by the algorithm, to avoid the loss of relevant individuals for the child generations. A suitable macro developed in the CFD software allows to automatically run all the different simulations, freezing the best configuration coming from each generation and move on with the next child generation in a series of evolutionary simulations. A total number of 75 simulations is needed to find the optimum. To prove the robustness of the algorithm developed here, a second optimization loop has been performed, following the same strategy highlighted above, but starting form an initial population which corresponds, for the passages 2-10 and 12-20, to the best configuration resulting from the first optimization loop.

4. Results of the flow optimization

In this section, the results of the simulations driven by the optimization algorithm are discussed.

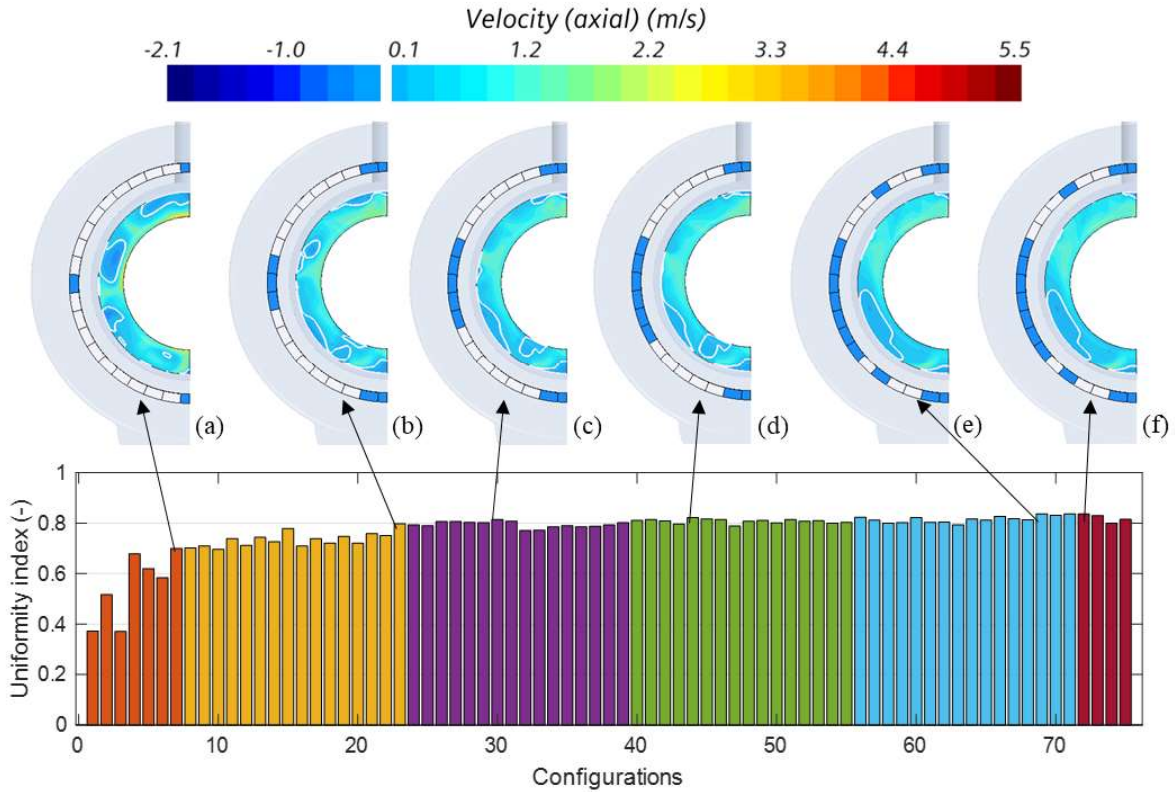

Figure 8 – Computed Uniformity Index for the different interface wall configurations resulting from the optimization algorithm applied to the first population. The different colors correspond to each child generation of the algorithm. On top: axial velocity distribution computed for the configuration resulting with the maximum UI for each child generation of the genetic algorithm: (a) configuration # 7 (UI = 0.700), (b) configuration # 23 (UI = 0.798), (c) configuration # 30 (UI = 0.814), (d) configuration # 44 (UI = 0.822), (e) configuration # 69 (UI = 0.836), (f) configuration # 72 (0.836). The white lines in the velocity maps separate the positive and the negative values of the velocity.

The value of UI for all the configuration analyzed in the first optimization loop is summarized in Figure 8. The best configuration corresponding to the highest UI, for each child generation of the first

population, also reported in Figure 8, show a progressive increase of the flow homogeneity on the surface at the inlet of the cavity region.

When the genetic algorithm is applied for the second time, the results of the new optimization loop, reported in Figure 9 for each child generation, shows a much smaller capability of all the different generations to further improve the UI. The corresponding flow field for the best configuration of each child generation, also reported in Figure 9, show a very similar velocity distribution (note that the color map is much reduced there, if compared to that in Figure 8), corresponding as expected to very similar interface wall configuration.

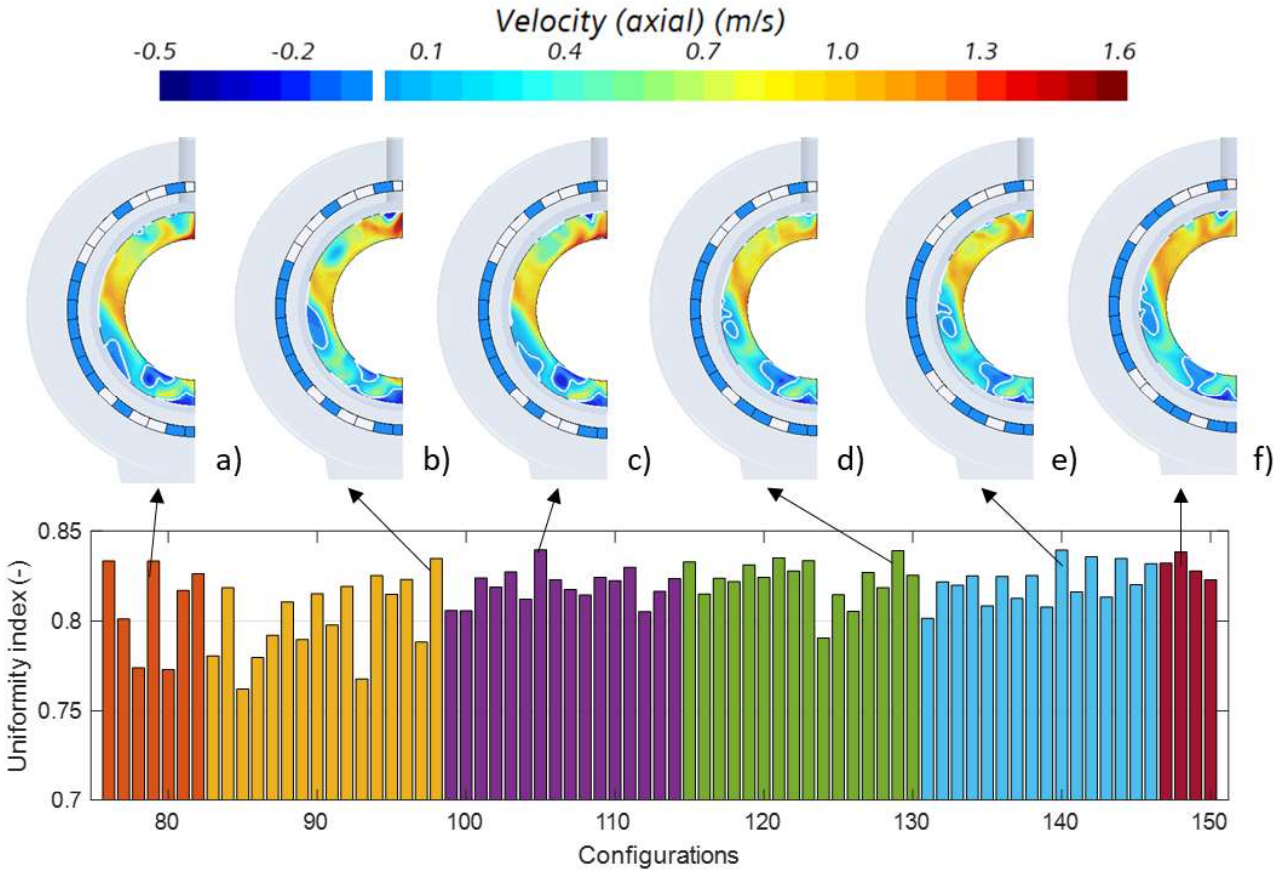

Figure 9 – Computed Uniformity Index for the different interface wall configurations resulting from the optimization algorithm applied to the second optimization loop (note that the y-axis has been zoomed in the range 0.7-0.85). On top: axial velocity distribution computed for the configuration resulting with the maximum UI for each child generation of the genetic algorithm: (a) configuration # 79 (UI = 0.833), (b) configuration # 98 (UI = 0.835), (c) configuration # 105 (UI = 0.839), (d) configuration # 129 (UI = 0.839), (e) configuration # 140 (UI = 0.839), (f) configuration # 148 (UI = 0.838). The white lines in the velocity maps separate the positive and the negative values of the velocity.

The overall optimal configuration results to be # 140, which presents smaller opening on top and bottom of the interface, while wide opening on the sides. The computed velocity field at the entrance of the RR region shows, with respect to the original TH1507U configuration, a significantly higher homogeneity, as can be seen from the comparison between Figure 6 and Figure 11a. Furthermore, if we look at the azimuthal distribution of the axial velocity computed for the original TH1507U design and for the optimized design, reported in Figure 11, a lower maximum-to-average velocity index can be computed: that index is 5.6 in the original configuration and ~1.2 in the optimized one, confirming the improvement of the flow homogeneity of the optimized design proposed here.

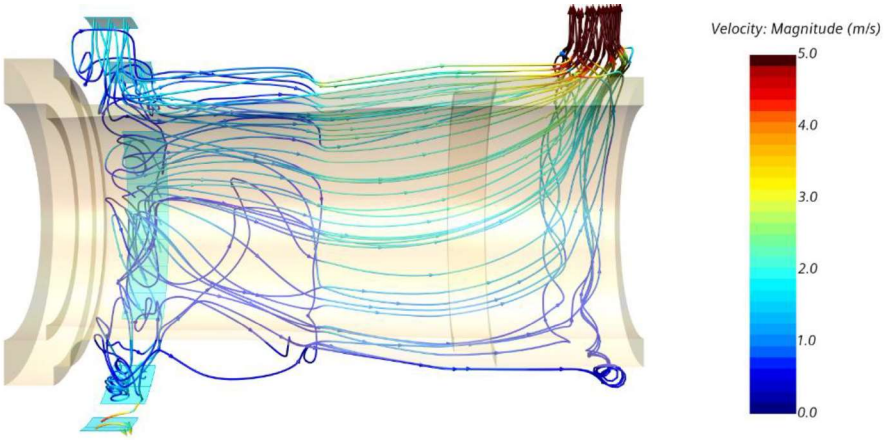

Figure 10 – Streamlines (45 lines distributed according the flow rate) colored by the value of the fluid velocity for the optimal configuration (#140) resulting from the optimization algorithm.

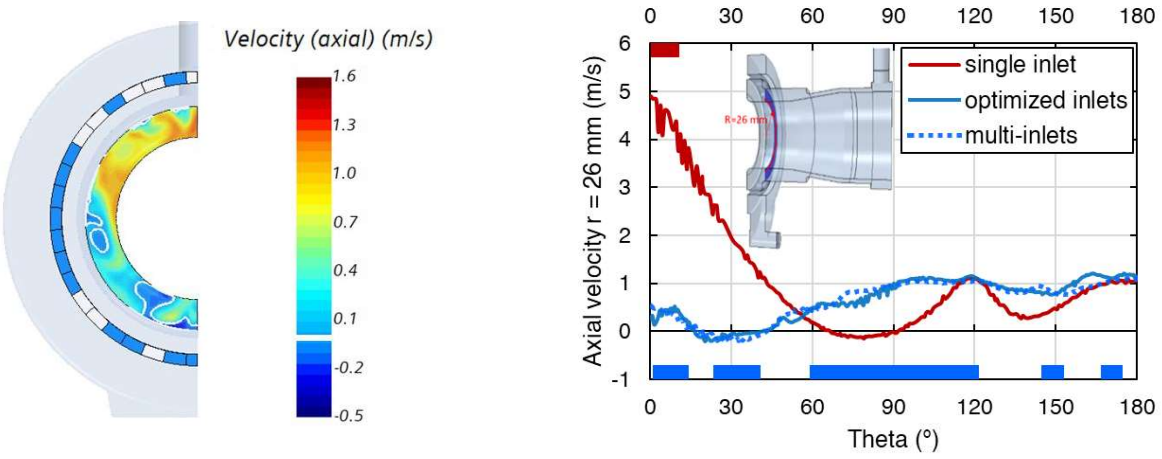

(a) (b)

Figure 11 – (a) Axial velocity distribution computed for the optimized design on the surface at the inlet of the high heat load region; The white lines separate the positive and the negative values of the velocity. (b) Azimuthal distribution of the axial velocity computed for the original TH1507U design (single inlet), for the optimized inlets design and for the engineered solution (multi-inlets) on the line shown in the sketch.

4.1 Engineered solution

The optimized solution has been engineered by substituting the open part of the interface wall, obtained from the optimization analysis, by rounded holes, which are "drilled" in the wall according to the constraints of:

- Keeping the position of the center of the area available for the fluid passage, in the interface wall frozen.
- Keeping the extension of the cross section available for the fluid passage, in the interface wall frozen.
- Keeping the depth of the area available for the fluid passage, in the axial direction frozen.

The resulting geometry is reported in Figure 12. It has been verified that the UI driven by the engineered solution is fully compliant with that computed above in the optimization process.

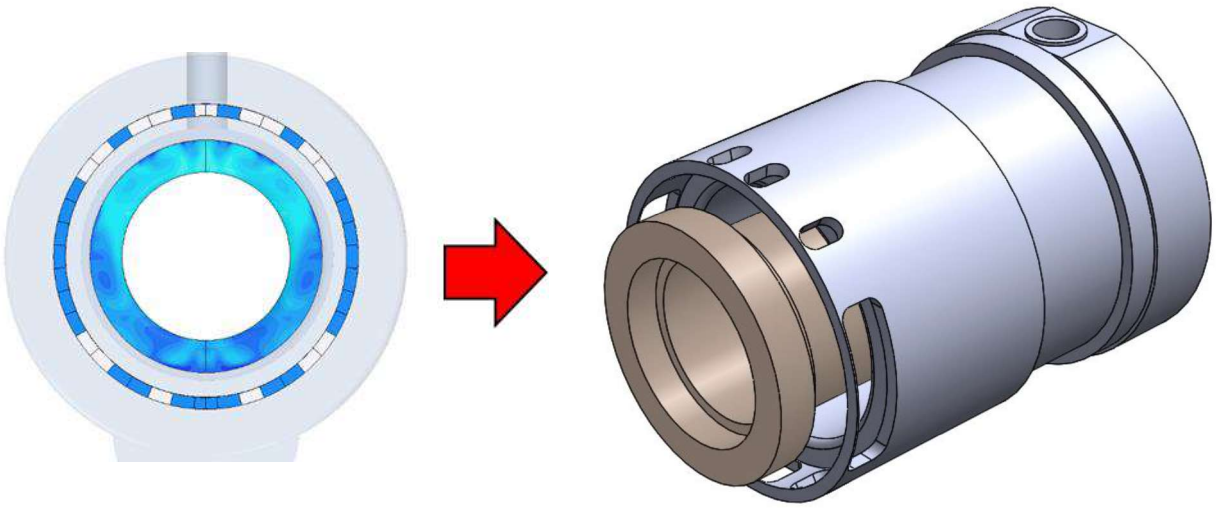

Figure 12 – Passage from the optimized configuration for the wall interface to an engineered design.

5. Exploiting flow acceleration to enhance the heat transfer

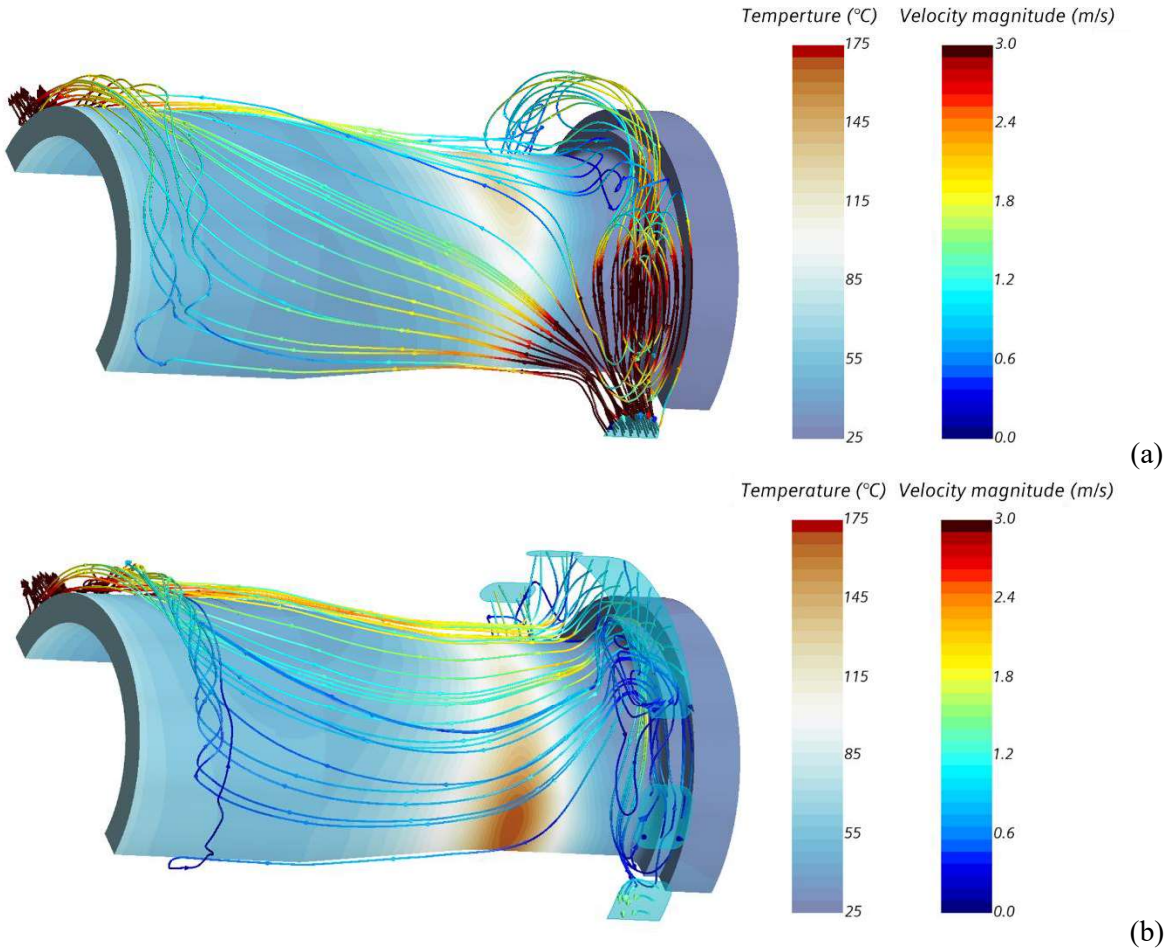

Figure 13 – Streamlines (45 lines distributed according the flow rate) colored by the value of the fluid velocity on the outer surface of the cavity colored in light blue-to-red by the surface temperature for the model with: (a) single inlet, (b) multiple inlets, as resulting from the optimization exercise above.

The effect on the cavity cooling of the multi-inlet configuration after the flow homogenization exercise can be assessed enriching the CFD model with the solid domain, shown in Figure 13, meshed using a polyhedral mesh with base size 0.6 mm in the high load region and 1.4 mm elsewhere. Copper, with temperature-dependent material properties is adopted in the simulation. The energy equation is solved in

steady-state both in the fluid and in the solid domains, through a segregated solver. The thermal driver used in the simulation is represented in Figure 2, with a peak value of 2580 kW/m^2. Note that the heat load adopted here is not relevant per se, since in the case study we do not model neither Raschig rings nor mini-channels, as in the actual devices, but it is still relevant from the point of view of the maximum temperature values reached in the most loaded zone of the cavity.

Figure 13 shows in a comparative fashion the axial velocity of the coolant in the cavity region, together with the temperature computed on the heated wall of the cavity, for the case of single inlet and optimized multi-inlets. In the first case, the temperature at the axial location of the peak load, and at the azimuthal location where the fluid from the inlet hits the cavity, is ~ 90 °C, and it reaches ~ 135 °C on the opposite side. In that case, the average speed of the fluid through the single inlet is quite high, ~8.6 m/s, resulting downstream in a quite non-uniform azimuthal distribution in the cavity, as discussed above. In the case with the multi-inlets as coming from the optimization exercise, the temperature at the axial location of the peak load varies between ~ 120 - 180 °C, and the thermal performance seems much worst that that originated in the single-inlet configuration, notwithstanding the much better flow homogeneity. In the multi-inlet configuration, in fact, the average speed of the fluid through the inlets is ~1.4 m/s, and the heat transfer coefficient for the coolant is significantly deteriorated all around the cavity.

A simple re-scaling of the flow cross section of the inlet holes to match the original average fluid speed as shown in Figure 14, corresponding to a reduction by a scaling factor of 0.15 (= 1.4 m/s / 8.6 m/s), has then been adopted to retrieve the original cooling capability of the fluid. In the multi-inlets the fluid gets the same acceleration originally achieved in the single inlet configuration, so that a similar heat transfer coefficient is reached, all around the cavity, though, see Figure 15.

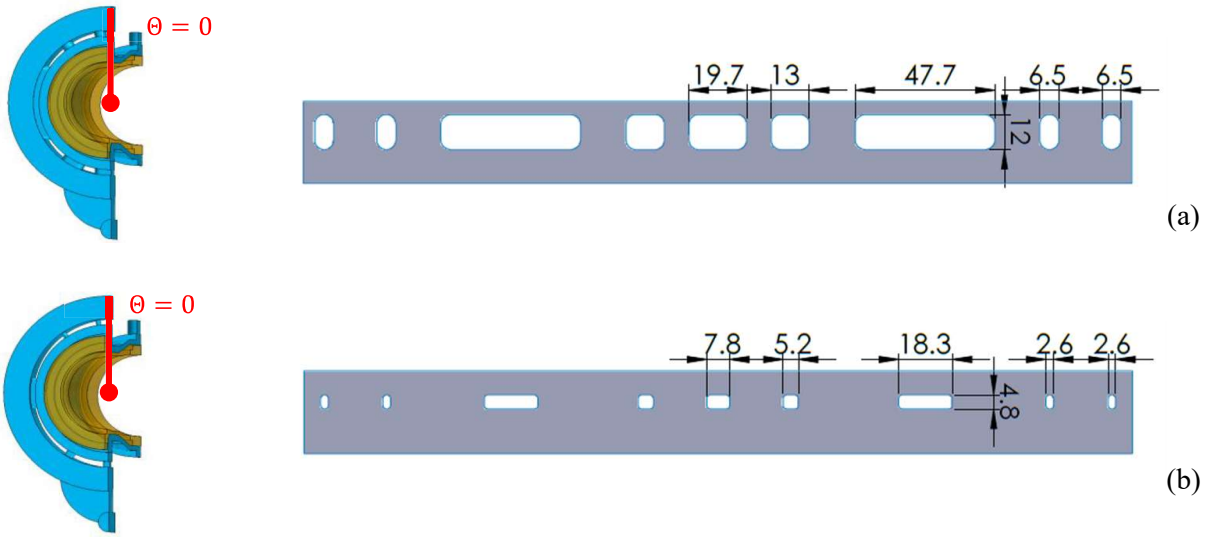

Figure 14 – Geometry and detail of the surface development of the interface wall between the distribution ring and the inlet mixing chamber for the two optimized-inlets solution: (a) planar plot of the interface for the model with original hole dimension, (b) planar plot of the interface for the model with reduced hole dimension.

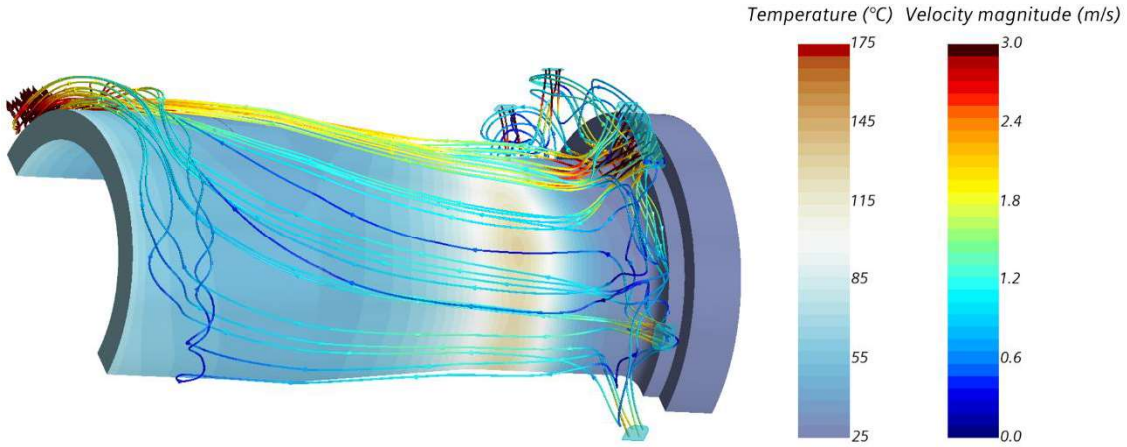

(c)

Figure 15 –Streamlines (45 lines distributed according the flow rate) colored by the value of the fluid velocity on the outer surface of the cavity colored in light blue-to-red by the surface temperature for the model with multiple inlets - small holes.

The final results of the design of the cavity inlet through the mini-multi inlet configuration are collected in Figure 16 in the form of azimuthal copper temperature and velocity profiles at the location of the peak heat load in Figure 2a, normalized with respect to the average values computed in the original case with a single inlet. While the velocity distribution around the cavity keeps at least the same level of uniformity of the configuration resulting from the multi-inlets with large holes (actually even better that that, since no negative values are faced anywhere), see Figure 16a, the temperature distribution is much more uniform, Figure 16b, with an average value lower than the configuration with a single inlet.

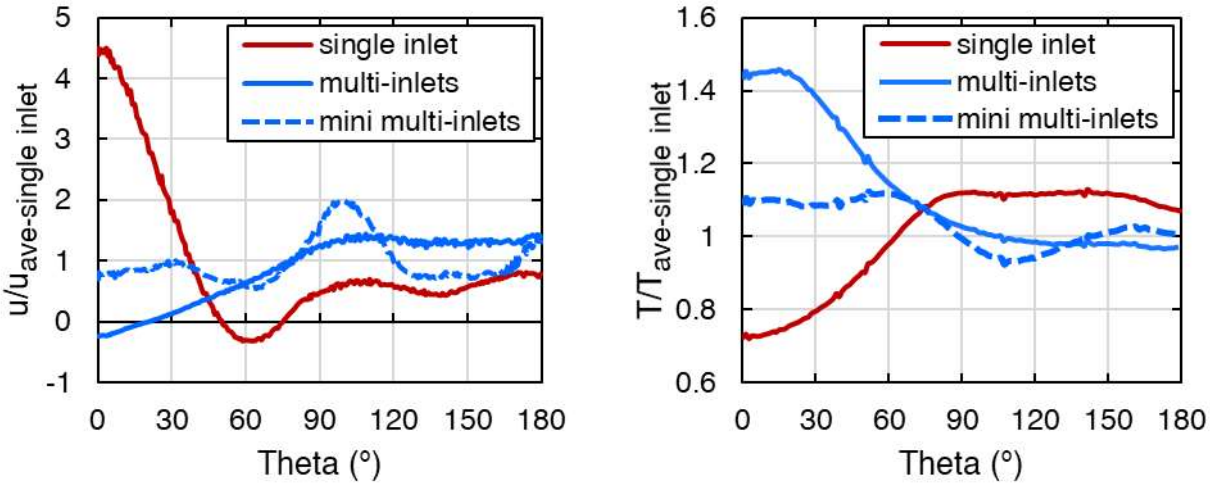

(a) (b)

Figure 16 – (a) Copper temperature on the heated surface, normalized on the mean azimuthal temperature of the single inlet cavity, computed on a section at x=31.65 mm, for the single inlet mode, previous model with large holes (multi-inlets), new model with reduced holes cross sections (mini multi-inlets). (b) Azimuthal distribution of the axial velocity, normalized on the azimuthally-averaged axial velocity of the single inlet cavity, for the same design of the figure at left.

6. Conclusions and perspective

The heat management is a crucial point in the development of new gyrotrons, and the capability to remove the heat deposited on the wall is the limiting factor in the cavity design. A new configuration for the coolant inlet to the cavity cooling region has been designed adopting an evolutionary algorithm for the

optimization of the location of the inlet passages from a distributing manifold, while the dimension of the passages has been tailored to reproduce the impinging jet effect, already beneficial for the heat removal in the present solution. The proposed solution, which can be easily implemented in conjunction with the mini-channel technology to provide even higher heat transfer capability, gives large confidence in addressing the future requirements, oriented to heat loads from 25 to 30 W/m^2.

References

[1] Erckmann V, Gasparino U. Electron cyclotron resonance heating and current drive in toroidal fusion plasmas. Plasma Phys Control Fusion 1994. https://doi.org/10.1088/0741-3335/36/12/001.

[2] Thumm MKA, Denisov GG, Sakamoto K, Tran MQ. High-power gyrotrons for electron cyclotron heating and current drive. Nucl Fusion 2019;59. https://doi.org/10.1088/1741-4326/ab2005.

[3] Singh U, Kumar N, Sinha AK. Gyrotron and its electron beam source: A review. J Fusion Energy 2012. https://doi.org/10.1007/s10894-011-9495-z.

[4] Thumm M. Recent advances in the worldwide fusion gyrotron development. IEEE Trans Plasma Sci 2014. https://doi.org/10.1109/TPS.2013.2284026.

[5] Aiello G, Scherer T, Avramidis K, Casal N, Franke T, Gagliardi M, et al. Diamond Window Technology for Electron Cyclotron Heating and Current Drive: State of the Art. Fusion Sci Technol 2019. https://doi.org/10.1080/15361055.2019.1643690.

[6] Manuilov VN, Morozkin M V., Luksha OI, Glyavin MY. Gyrotron collector systems: Types and capabilities. Infrared Phys Technol 2018. https://doi.org/10.1016/j.infrared.2018.03.024.

[7] Wu C, Pagonakis IG, Gantenbein G, Illy S, Thumm M, Jelonnek J. Conceptual designs of E × B multistage depressed collectors for gyrotrons. Phys Plasmas 2017. https://doi.org/10.1063/1.4979291.

[8] Avramidis KA, Gantenbein G, Ioannidis ZC, Pagonakis IG, Rzesnicki T, Thumm M, et al. Numerical studies on the influence of cavity thermal expansion on the performance of a high-power gyrotron. IVEC 2017 - 18th Int. Vac. Electron. Conf., 2018. https://doi.org/10.1109/IVEC.2017.8289512.

[9] Gyrotron n.d. https://www.britannica.com/technology/gyrotron.

[10] Jelonnek J, Aiello G, Alberti S, Avramidis K, Braunmueller F, Bruschi A, et al. Design considerations for future DEMO gyrotrons: A review on related gyrotron activities within EUROfusion. Fusion Eng Des 2017. https://doi.org/10.1016/j.fusengdes.2017.01.047.

[11] Kariya T, Minami R, Imai T, Okada M, Motoyoshi F, Numakura T, et al. Development of high power gyrotrons for advanced fusion devices. Nucl Fusion 2019. https://doi.org/10.1088/1741-4326/ab0e2c.

[12] Jelonnek J, Aiello G, Albaiar F, Alberti S, Avramidis KA, Bertinetti A, et al. From W7-X Towards ITER and Beyond: 2019 Status on EU Fusion Gyrotron Developments. 2019 Int. Vac. Electron. Conf. IVEC 2019, 2019. https://doi.org/10.1109/IVEC.2019.8744989.

[13] Kumar N, Kumar A, Singh U, … TS-IJ of, 2011 U. Thermal and Structural Analysis of Interaction Cavity and Its Effect on the Operating Mode Excitation for a 120áGHz, 1áMW Gyrotron. Int J Thermophys 2011;32:1038–46. https://doi.org/10.1007/s10765-011-0963-5.

[14] Koner J, Bera A, Sinha AK. Study of thermal effects on 200kW, 42GHz gyrotron cavity. 2008 Int Conf Recent Adv Microw Theory Appl Microw 2008 2008:190–1. https://doi.org/10.1109/AMTA.2008.4763162.

[15] Bertinetti A, Avramidis KA, Albajar F, Cau F, Cismondi F, Rozier Y, et al. Multi-physics analysis of a 1 MW gyrotron cavity cooled by mini-channels. Fusion Eng Des 2017;123:313–6.

https://doi.org/10.1016/J.FUSENGDES.2017.05.016.

[16] Karmakar S, Sudhakar R, Mudiganti JC, Seshadri R, Kartikeyan M V. Electrical and Thermal Design of a W-Band Gyrotron Interaction Cavity. IEEE Trans Plasma Sci 2019;47:3155–9. https://doi.org/10.1109/TPS.2019.2918138.

[17] Marchesin R, Albert S, Avramidis KA, Bertinetti A, Dubrav J, Fascl D, et al. Manufacturing and Test of the 1 MW Long-Pulse 84/126 GHz Dual-Frequency Gyrotron for TCV. 2019 Int Vac Electron Conf IVEC 2019 2019. https://doi.org/10.1109/IVEC.2019.8745147.

[18] Leggieri A, Albajar F, Alberti S, Allio A, Avramidis KA, Bariou D, et al. Upgrade of The European ITER 170 GHz 1 MW CW Industrial Gyrotron (TH1509). 7th IVEW 2020 13th IVeSC 2020, 2020.

[19] Leggieri A, Albajar F, Albert S, Allio A, Avramidis KA, Bariou D, et al. TH1509U European 170 GHz 1 MW CW Industrial Gyrotron Upgrade. IEEE IVEC 2021, 2021.

[20] Avramidis KA, Ioannidis ZC, Aiello G, Bénin P, Chelis I, Dinklage A, et al. Towards a 1.5 MW, 140 GHz gyrotron for the upgraded ECRH system at W7-X. Fusion Eng Des 2021;164:112173. https://doi.org/10.1016/J.FUSENGDES.2020.112173.

[21] Leggieri A, Alberti S, Avramidis KA, Dammertz G, Erckmann V, Gantenbein G, et al. THALES TH1507 140 GHz 1 MW CW gyrotron for W7-X stellarator. Int Conf Infrared, Millimeter, Terahertz Waves, IRMMW-THz 2019;2019-September. https://doi.org/10.1109/IRMMW-THZ.2019.8874589.

[22] Leggieri A, Allio A, Difonzo R, Legrand F, Marchesin R, Savoldi L. Système électronique muni d'un circuit de refroidissement à fluide caloporteur. Patent Application 2110917, 2021.

[23] Menter FR. Zonal two equation κ-ω turbulence models for aerodynamic flows. AIAA 23rd Fluid Dyn. Plasmadynamics, Lasers Conf. 1993, 1993. https://doi.org/10.2514/6.1993-2906.

[24] Siemens PLM Software Inc. Star-CCM+ User's Guide v. 15.02 2020.